2-D tomography of volcanic CO₂ from scanning hard target differential absorption LIDAR: The case of Solfatara, Campi Flegrei (Italy)

Manuel Queiβer[1], Domenico Granieri[2], Mike Burton[1]

[1]School of Earth, Atmospheric and Environmental Sciences, University of Manchester, Oxford Road, Manchester M13 9PL, UK
[2]Istituto Nazionale di Geofisica e Vulcanologia (INGV), Sezione di Pisa, 50126 Pisa, Italy

Correspondence to: Manuel Queiβer (manuel.queisser@manchester.ac.uk), Tel.: +44(0)161 2750778, Fax.: +44(0)161 306 9361

Abstract. Solfatara is part of the active volcanic zone of Campi Flegrei (Italy), a densely populated urban area where ground uplift and increasing ground temperature are observed, connected with rising rates of CO_2 emission. A major pathway of CO_2 release at Campi Flegrei is diffuse soil degassing, and therefore quantifying diffuse CO_2 emission rates is of vital interest. Conventional in-situ probing of soil gas emissions with accumulation chambers is accurate over a small footprint but requires significant time and effort to cover large areas. An alternative approach is differential absorption LIDAR, which allows for a fast and spatially integrated measurement. Here, a portable hard-target differential absorption LIDAR has been used to acquire horizontal 1-D profiles of CO_2 concentration at the Solfatara crater. To capture the non-isotropic nature of the diffuse degassing activity, a 2-D tomographic map of the CO_2 distribution has been inverted from the 1-D profiles. The acquisition was performed from a single half space only, which increases the non-linearity of the inverse problem. Nonetheless, the result is in agreement with independent measurements and furthermore confirms an area of anomalous CO_2 degassing along the eastern edge as well as the center of the Solfatara crater. The method has important implications for measurements of degassing features that can only be accessed from limited angles, such as airborne sensing of volcanic plumes. CO_2 fluxes retrieved from the 2-D map are comparable, but modestly higher than emission rates from previous studies, perhaps reflecting a more integrated measurement.

1 Introduction

Subaerial volcanoes emit a variety of gaseous species, dominated by water vapor and CO_2, and aerosols. Originating from exsolution processes that may take place deep in the crust due to the low solubility of CO_2 in magmas, volcanic CO_2 is a powerful tracer for magmatic recharge and ascent processes (Burton et al., 2013; Frezzotti et al., 2014; Chiodini et al., 2015; La Spina et al., 2015). Measuring volcanic CO_2 emission rates is therefore also a feasible pathway towards improved forecasting of volcanic activity, such as seismicity or eruptions (Petrazzuoli et al., 1999; Carapezza et al. 2004; Aiuppa et al.,

2011). Unfortunately, magmatic CO_2 is not only released actively via vents such as the volcano mouth, but also diffusively via soil or flank degassing (Baubron et al., 1991; Hards, 2005; Chiodini et al., 2007). In addition, in most cases the volcanic CO_2 signal is modest compared with ambient concentrations (Burton et al., 2013) and quickly diluted into the atmosphere. A common approach to determine the magmatic CO_2 flux is based on a gridded sampling of the CO_2 distribution in the volcanic

5   plume itself (Gerlach et al., 1997; Lewicki et al., 2005; Diaz et al., 2010; Lee et al., 2016) from which 2-D CO_2 concentration maps are retrieved by secondary data processing, such as statistical methods (Lewicki et al., 2005; McGee et al., 2008) and dispersion modeling (Aiuppa et al., 2013; Granieri et al., 2014). Integrating the CO_2 concentrations over the cross sectional plume area and multiplying the result with the transport speed perpendicular to the cross section yields CO_2 fluxes. The in situ method has two drawbacks. Firstly, it may be dangerous to perform in situ measurements from within the volcanic plume (e.g.

10   due to toxic gases or low visibility near the crater mouth). Secondly, in situ methods allow for a very accurate estimation of CO_2 concentration, but only in the vicinity of the measurement point, potentially missing significant contributions from in between the measurement points.

      Remote sensing techniques (see Platt et al., 2015 for overview of state-of-the-art), notably active remote sensing platforms, including differential absorption LIDAR (DIAL) and spectrometers (Menzies and Chahine, 1974; Weibring et al.,

15   1998; Koch et al., 2004; Kameyama et al., 2009) acquire columns of range resolved (Sakaizawa et al., 2009; Aiuppa et al., 2015) or column averaged (Amediek et al., 2008; Kameyama et al., 2009) CO_2 concentrations. They provide a powerful tool to overcome the aforementioned drawbacks of in situ measurement techniques by offering a faster, safer and comprehensive acquisition (spatial coverage yields inclusive CO_2 concentration profiles). Moreover, there is no need for receivers or retroreflectors at the opposite end of the measurement column, which increases not only flexibility and timeliness of the

20   acquisition, but is crucial for some measurements, including airborne or spaceborne acquisitions.

      Active remote sensing platforms based on hard target DIAL (topographic target DIAL) can use continuous wave lasers. This allows for high signal return and compact, rugged and portable instruments, which is desirable for platform independent measurement of atmospheric CO_2, be it ground based or air-borne (Sakaizawa et al., 2013; Queißer et al., 2015a). Yet, the drawback compared with "traditional", pulsed DIAL is that no range resolved CO_2 concentrations are measured, but

25   column densities (in m^{-2}) or, as in this work, path length concentration products (called "path amount" hereafter, in ppm.m). By scanning across the emission feature one obtains 1-D profiles of path amounts. Using these profiles to determine CO_2 fluxes is straightforward only for gas plumes for which a homogeneous cross section can be assumed (Galle et al., 2010). However, particularly diffuse degassing activities are often not associated with homogeneous, but an unknown CO_2 distribution within the scanned plume cross section. Therefore, the assumption of homogenous CO_2 distribution may lead to

30   under or overestimated CO_2 fluxes when probed from different directions, since path amounts are measured, which represent path averaged CO_2 concentrations. It would be very desirable, and this was the main motivation of this work, to have a 2-D map that at least contains the geometry of the anomalous CO_2 release, let aside precise CO_2 mixing ratios. This would allow to geometrically correct the fluxes derived from CO_2 path amounts delivered by hard target DIAL systems. Provided the 2-D map contains correct CO_2 mixing ratios, the CO_2 flux can be conveniently obtained by simple integration over the 2-D map.

Note that tomographic reconstructions of volcanic gas plumes have already been performed, however, for SO_2 and using passive remote sensing techniques (Kazahaya et al., 2008; Wright et al., 2008; Johansson et al., 2009).

The study was focusing on a zone of diffuse degassing of magmatic CO_2 within the Solfatara crater (Italy) reported previously (e.g. Bagnato et al., 2014). Solfatara is a fumarolic field and part of the active volcanic area of Campi Flegrei (CF, Fig. 1). CF is a nested caldera, resulting from two large collapses, the last one ~15 ka ago (Scarpati et al., 1993). CF is in direct vicinity to the metropolis of Naples and thus a direct threat to millions of residents. Thanks to its accessibility and strong CO_2 degassing Solfatara provides almost a model like volcano, a natural laboratory, to test new sensing approaches. On the other hand, it is part of one of the most dangerous volcanic zones in the world, showing ground uplift coupled with seismic activity with magma degassing likely having a significant role in triggering unrest (Chiodini at al., 2010). Solfatara therefore merits particular monitoring efforts and any new results on observables, may they stem from well-tried or new methods, are of direct importance to understand the fate of this active volcanic system.

2 Methods

2.1 Measuring 1-D profiles of CO_2 path amounts

The CO2DIAL (Fig. 2) is an active remote sensing platform based on the differential absorption LIDAR principle (Koch et al., 2004; Amediek et al., 2008). It is a further development of the portable instrument described in Queißer et al. (2015a, 2015b). By taking the ratio of the optical powers associated with the received signals for the wavelengths coinciding with an absorption line of CO_2 and the wavelength at the line edge, λ_{ON} and λ_{OFF}, respectively, one arrives at

$$2 \int_0^R dr \Delta\sigma(r) N_{CO_2}(r) = -\ln\left(\frac{P(\lambda_{ON})P(\lambda_{OFF})_{ref}}{P(\lambda_{OFF})P(\lambda_{ON})_{ref}}\right), \qquad (1)$$

$$\equiv \Delta\tau$$

where N_{CO_2} is the CO_2 number density, R is the range, i.e. the distance between the instrument and the hard target, $\Delta\sigma$ is the difference between the molecular absorption cross sections of CO_2 associated with λ_{ON} and λ_{OFF}, $P(\lambda)$ is the received ("science") and $P(\lambda)_{ref}$ the transmitted optical power ("reference"). The latter is measured as a reference to normalize fluctuations of the transmitted power. The normalized optical power in Eq. (1) is referred to as grand ratio (GR),

$$GR = \frac{P(\lambda_{ON})P(\lambda_{OFF})_{ref}}{P(\lambda_{OFF})P(\lambda_{ON})_{ref}} \qquad (2)$$

$\Delta\tau$ is the differential optical depth. The two distributed feedback (DFB) fiber seed lasers emit at λ_{ON}=1572.992 nm and λ_{OFF}= 1573.173 nm (Rothman et al., 2013). To be able to easily reject background noise (such as solar background) lock-in detection is used. Consequently, both seed laser beams (for λ_{ON} and λ_{OFF}) are amplitude modulated using two $LiNbO_3$ electro-optical modulators (EOM) at slightly different sine tones near 5 kHz and simultaneously amplified by an Erbium doped fiber amplifier (EDFA) before being transmitted. The transmitted optical power can be adjusted between ~80 mW and a maximum of 1.5 W. A glass wedge scatters a fraction of the transmitted light into an integrating sphere where the reference detector is mounted.

The transmitted light is diffusively backscattered by a hard target, which can be any surface located up to ~2000 m away from the instrument, and is received by a 200 mm diameter Schmidt-Cassegrain Telescope with a focal length of 1950 mm. Typically the received optical power is a couple of nW at a bandwidth integrated noise of ~1 pW (root mean squared noise equivalent power). The analog to digital converter (ADC) operates at 250 kSamples s^{-1} and has a resolution of 16-bit. The integration
5   time per scan angle was set to 4000 EOM modulation periods, which corresponds to data chunks of length 784 ms (integration time) for both science and reference channel. Each of these four chunks of data is demodulated using a digital lock-in routine following Dobler et al. (2013). After the lock-in operation one arrives at four DC signals, associated with the optical powers $P(\lambda_{ON})$, $P(\lambda_{OFF})$, $P(\lambda_{ON})_{ref}$ and $P(\lambda_{OFF})_{ref}$. $\Delta\tau$ is calculated using the right hand side of Eq. (1), after taking the mean of each of the four signals. To account for the instrumental offset of $\Delta\tau$, prior to scanning the volcanic plume, values of $\Delta\tau$ were
10   acquired for different R in the ambient atmosphere. The points were used to fit a calibration curve. The ordinate at R=0 gave the instrumental offset. The calibration curve was also used to convert the measured in-plume $\Delta\tau$ to CO_2 path amounts $X_{CO_2}{}^{col}$ (in ppm.m). Column averaged CO_2 mixing ratios $X_{CO_2,av}$ (in ppm) were obtained by dividing path amounts by R. The range was measured by an onboard range finder (DLEM, Jenoptik, Germany), based on a 1550 nm LIDAR with pulse energy of 500 μJ and accuracy <1 m. By pivoting the receiver/transmitter unit using a step motor values for $X_{CO_2}{}^{col}$ (or $X_{CO_2,av}$) per heading
15   were attained, and hence 1-D profiles.

The precision of the column averaged CO_2 mixing ratio was evaluated as

$$\left(\frac{\Delta X_{CO_2,av}}{X_{CO_2,av}}\right)^2 = SNR^{-2} + \left(\frac{\sigma_R}{\langle R \rangle}\right)^2 + \delta_{Speckle}{}^2, \tag{3}$$

with the signal-to-noise-ratio (SNR)

$$SNR = \left[\frac{\sigma_{GR}}{\langle GR \rangle}\frac{1}{\ln(\langle GR \rangle)}\right]^{-1}, \tag{4}$$

20   where $\langle GR \rangle$ and σ_{GR} are the mean and standard deviation of the grand ratio, respectively. They were estimated from time series acquired at fixed angles in between the scans at CF. The SNR accounts for all noise sources occurring during acquisition, including instrumental noise, non-stationary baseline drift, solar background noise, atmospheric noise (mostly air turbulence) and perturbation by aerosol scattering (e.g. condensed water vapor). The second term depicts the relative range uncertainty (standard deviation of ranges σ_R over mean of ranges $\langle R \rangle$) which is typically ~1 m. The relative uncertainty due to hard target
25   speckle was estimated as (MacKerrow et al., 1997)

$$\delta_{Speckle} = \frac{1.22\lambda_{OFF}R}{D\xi}, \tag{5}$$

where D is the spot diameter on the hard target (in m) and ξ is the dimension of the telescope field of view (in m) on the hard target.

2.2 Reconstructing a 2-D CO₂ concentration map

Ranges and their respective heading angles (i.e. range vectors, referred to as rays in the following) from the scans were converted to absolute Cartesian coordinates (x, y). The goal is to obtain CO_2 mixing ratios (X_{CO_2}, in ppm) at a given point (x, y). Due to the finite spatial resolution of every measurement system this will always be an average mixing ratio within a confined space, in this case a 2-D grid cell. The region of interest (area bounding the scans) was divided into grid cells with length Δx (in x direction) and Δy (in y direction). X_{CO_2} were inferred from the measured $X_{CO_2}{}^{col}$ using an inverse technique following Pedone et al. (2014). Thereby one uses the fact that the CO_2 path amount is associated with the product of a range segment and a uniform CO_2 mixing ratio X_{CO_2} along that range segment. For a given ray and for n grid cells traversed by the ray this can be written as

$$\sum_{i=1}^{n} r_i X_{CO_2,i} = X_{CO_2}{}^{col}, \qquad (6)$$

where r_i depicts the length of the ray segment in grid cell i ($\sum_{i=1}^{n} r_i = R$). $X_{CO_2,i}$ is the (unknown) CO_2 mixing ratio within grid cell i (in ppm). Including all rays, one arrives at a system of linear equations, which can be written as

$$Lc = a, \qquad (7)$$

where L is a $m \times n$ matrix, called geometry matrix, containing all m rays for all n grid cells, c is a $n \times 1$ matrix containing the uniform X_{CO_2} per grid cell and is the desired quantity to be inverted. a is a $m \times 1$ matrix containing the measured (observed) $X_{CO_2}{}^{col}$ for each ray. For simplicity, $n_x = n_y$, where n_x, n_y are the number of grid cells in x- and y-direction, respectively. Thus, $n = n_x{}^2$.

To invert Eq. (7) for c a least square solver, the MATLAB LSQR routine, was used. The algorithm iteratively seeks values for c, which minimize the misfit $\|a - Lc\|$. Therefore, c represents a model with a maximized likelihood of explaining the observed data a. By reshaping c into the measurement 2-D grid a 2-D map was obtained.

2.3 CO₂ flux retrieval

From the inverted 2-D map of X_{CO_2} the CO_2 flux was computed as

$$\phi_{CO_2} = 10^{-6} u N_{air} \frac{M_{CO_2}}{N_A} \iint_{plume} dx dy \, X_{CO_2,pl}(x, y) \qquad (8)$$

where $X_{CO_2,pl}$ are the inverted, background corrected CO_2 mixing ratios computed as

$$X_{CO_2,pl}(x, y) = X_{CO_2}(x, y) - X_{CO_2,bg}, \qquad (9)$$

where $X_{CO_2,bg} = 380$ ppm is the background CO_2 mixing ratio at Solfatara measured in situ. u is the magnitude of the component of the plume transport speed perpendicular to the scanned cross section (in m s⁻¹), N_{air} is the number density of air (in m⁻³), computed using meteorological data (pressure, temperature, humidity) acquired by a portable meteorological station close to the instrument. M_{CO_2} is the molar mass of CO_2 (in kg mol⁻¹) and N_A is Avogadro's constant (in mol⁻¹).

The plume transport speed was evaluated from digital video footage acquired during the measurement, employing a video analysis program (Tracker from Open Source Physics). Condensed water vapor aerosol emitted by various vents in the region of interest was assumed to propagate with the same velocity as the volcanic CO_2. At a given video frame a pixel was fixed and the calibrated propagated distance (in pixels) was measured as the video proceeded. Since the frame rate of the video was known (30 frames per second), the speed by which the tracked point and hence a parcel of gas was transported could be estimated.

The relative error of the CO_2 flux was estimated as

$$\left(\frac{\Delta\phi_{CO_2}}{\phi_{CO_2}}\right)^2 = \left(\frac{\Delta u}{u}\right)^2 + \left(\frac{\iint_{plume} dxdy\, \Delta X_{CO_2,pl}(x,y)}{\iint_{plume} dxdy\, X_{CO_2,pl}(x,y)}\right)^2,$$

(10)

where $\Delta X_{CO_2,pl}$ is the absolute error of the CO_2 mixing ratio at a given point within the integrated area and Δu is the absolute uncertainty of the plume speed.

3 Results

The experiment took place on 4 March 2016 inside the crater of Solfatara (Fig. 1) and was focusing on the diffuse CO_2 release alongside the Solfatara crater edge, located south of the main vents Bocca Nuova (BN) and Bocca Grande (BG), although they were included in the scans. Elevated CO_2 mixing ratios, up to 1500 ppm at places, could be affirmed by means of in situ measurements using a LICOR CO_2 analyzer with 4% accuracy. The LICOR analyzer was measuring at the same height as the propagation height of the laser beam (ca. 2 m above ground). Due to logistical constraints the in situ measurements could only be measured the day before the experiment. Five scans were performed between 9:35 and 11:57 LT (duration 142 min) from five different locations with a total of $m = 627$ beam paths (rays), which are shown along with the respective five instrument locations in Fig 1c. It is assumed that during the complete acquisition the CO_2 distribution did not change ("frozen plume"). For each scan and for each heading differential optical depths $\Delta\tau$ have been retrieved and converted into $X_{CO_2}{}^{col}$ (and $X_{CO_2,av}$), as detailed in the method section. The resulting 1-D concentration profiles are shown in Fig. 3. Numerous wiggles indicate vigorous degassing activity, suggesting diffuse degassing or CO_2 advected by local wind eddies. In addition, there are symmetric features, such as around 26° in Fig. 3a, which appeared in scans carried out prior to the experiment and the day before, thus suggesting vented degassing activity. The angular scanning velocity was 2.1 mrad s^{-1}, associated with an angular resolution of 1.65 mrad, which corresponds to a lateral resolution of around 24 cm between points in Fig. 3.

To invert for X_{CO_2}, ranges and headings were converted to Cartesian coordinates. The coordinate system was chosen such that the instrument positions of all five scans were located on the y-axis (Fig. 1c). It proved to be useful to plot the measured data, i.e. $X_{CO_2,av}$ against their associated coordinates. The result (Fig. 4) is a semi-quantitative map indicating where high CO_2 concentrations are likely to be expected. This image therefore provides valuable a-priori information for the inversion.

The LSQR algorithm was tested using a synthetic realistic scenario. Synthetic data $X_{CO_2}{}^{col}$ were generated from a true model comprising of known X_{CO_2} at each grid point using the real geometry matrix L, which contained the actual instrument positions and measured ranges. X_{CO_2} of the true model were starting at 380 ppm at grid 1 and increasing by 60 ppm per increase in grid number (Fig. 5a). By running the inversion with varying number of grid cells the viable number of grid

5 cells was found to be between $n = 4$ up to 36 without considerable loss of capability to recover the true X_{CO_2} (Fig. 5b). For $n > 36$ the inverted X_{CO_2} oscillated, that is, they were over and under shooting the true X_{CO_2}.

For the real data, however, already for $n > 16$ the inversion yielded unreasonable high X_{CO_2}, indicating an oscillation. The inverse problem is over determined since $m \gg n$, i.e. the number of beam paths traversing most of the grid cells is much higher than any practical number of grid cells usable for the inversion. Increasing the number of grid cells would

10 reduce the number of rays traversing a given grid cell, but the problem would become highly non-linear. Generally, a viable strategy to tackle non-linearity in situations like that is a gradual introduction of non-linearity, such as by splitting up the inversion into sub-steps, using a starting model close enough to the true solution at each step (Queißer et al., 2012). With each increase in sub-step, the starting model contains more small-scale information. This approach was tested in the real data inversion. Starting with $n = 4$ grid cells, the inversion result was interpolated, smoothed and used as the starting model for the

15 inversion with $(n_x + 1)^2$ grid cells. At $n = 25$ the location of the peak X_{CO_2} were in strong disagreement with the LICOR data, indicating that the inversion was trapped in a local minimum. A similar outcome was obtained by reducing the number of rays used for the inversion (using every 2nd up to every 10th ray).

That left $n = 16$ the maximum feasible number of grid cells for a robust inversion. The resulting grid length was $\Delta x = 38$ m and $\Delta y = 33$ m. As for the synthetic tests, a constant X_{CO_2}, the mean of the raw data (Fig. 4), was used as a starting

20 model. The inversion result is shown in Fig. 6a. To increase spatial resolution the inverted model was interpolated onto a grid with grid spacing $\Delta x/8$ and $\Delta y/8$ using ordinary Kriging interpolation (Oliver, 1996). The result is shown in Fig. 6b. Overlaying the 2-D map of CO_2 mixing ratios with the map of Solfatara reveals a zone of increased anomalous CO_2 degassing activity along the southeastern edge of Solfatara, which is in reasonable agreement with in situ data from the LICOR CO_2 analyzer (Fig. 6c).

25 The resulting 2-D map of CO_2 mixing ratios was used to compute the CO_2 flux. Since zones with poor ray coverage were prone to inversion artifacts (see Fig. 4c) zones without ray coverage were excluded from integration. The plume transport speed was estimated to be 1.1 ± 0.2 m s^{-1}. The plume speed uncertainty was retrieved from the standard deviation of various plume speeds retrieved from different tracks carried out across the plume. To estimate the flux uncertainty (Eq. 10), a constant $\Delta X_{CO_2,pl} = \max(\Delta X_{CO_2,av})$ was considered (maximum error of all five scans). Using Eq. (8) the resulting CO_2 flux was

30 computed as 12.8 ± 3.3 kg s^{-1} (± 1 SD) or 1106 ± 288 tons day^{-1}.

4 Discussion

The retrieved 2-D map (Fig. 6c) indicates an elongated zone of intense anomalous degassing along the eastern edge of the Solfatara crater. Encouragingly, this is a persistent feature in different inversions performed with different number of grid cells and beam paths (and thus degree of non-linearity) and underpins that it is real. Previous measurements sampling the Solfatara area with accumulation chambers yielded an increased anomalous CO_2 degassing activity in the corresponding area too (Granieri et al., 2010; Tassi et al., 2013; Bagnato et al., 2014). The retrieved elongated zone of anomalous CO_2 degassing likely encompasses at least two major vents (Fig. 6c). The locations of the peaks in CO_2 mixing ratio in Fig. 6c fairly agree with the 1-D input data. For instance, the peak near the center of the crater corresponds to the peak near 26° in the first scan in Fig. 3a. The second scan (Fig. 3b) indicates a rather abrupt decrease in $X_{CO_2,av}$ at 28°, in line with the edge of the zone of elevated CO_2 concentrations at the crater center (Fig. 6c). This central degassing feature is coherent with results of recent campaigns (Granieri et al., 2010; Tassi et al., 2013; Bagnato et al., 2014). The symmetric increase in $X_{CO_2,av}$ near 9° in Fig. 3d corresponds to the position of the local peak in X_{CO_2} between in situ points 7 and 8 in Fig. 6c. Provided sufficient ray coverage and angle diversity, which is the case for the zones away from the edges of the 2-D map, disagreement between the peaks in the 1-D data (Fig. 3) and those in the 2-D map (Fig. 6) are likely due to physical fluctuations in CO_2 concentration. The plume was assumed to be "frozen", but the measurement duration of 142 min was certainly larger than the time scale of alterations in the dispersion pattern of the plume. During acquisition one could visually identify at least 5 small vents emitting water vapor and therefore most likely also CO_2. Though not recovered due to the limited spatial resolution of the inversion this advocates that there are in fact separate vents south of the main vents, near the edge of the Solfatara crater.

Retrieved X_{CO_2} peak near 1300 ppm (2 m above ground), in line with the in situ LICOR data, although not spatially matching them in places. Again, this can be explained by the fact that the in situ values were acquired the day before so that local wind and thus dispersion patterns were different. Nevertheless, both the LICOR in situ data and the inversion result indicate high X_{CO_2} near the main vents and along the crater edge. Near the main vents highest CO_2 mixing ratios in the 2-D map are located ca. 20 m west of BN. In fact, the whole zone of high X_{CO_2} is shifted 20 m northwest from where one would expect it. Since the predominant wind direction at the time of acquisition was around 300°, to first order one would expect the CO_2 to disperse rather towards southeast, along the crater edge. The main vent area was at the edge of the scanned area. Note that the relative inversion residual $\|a - Lc\|/\|a\|$ was 0.18, which means on average 18% of $X_{CO_2}{}^{col}$ are unexplained by the model in Fig. 6a. This mismatch is therefore likely due to poor ray coverage and angle diversity for the zone containing the main vents, since the acquisition focused on the zone south of the main vents. Possibly, but less likely, CO_2 was advected slightly towards west due to dispersive mechanism related to local wind eddies decoupled from the main wind direction. These dispersive mechanisms take place in any case and make a distinction between CO_2 from the main vents and the surrounding diffuse degassing challenging. For that reason, in future acquisitions at that site the region of interest shall be scanned from instrument positions aligned along a half circle around the zone rather than using a "flat" scan geometry as chosen here.

For a comparison, CO_2 fluxes were computed directly from the 1-D profiles, that is, similar to Eq. (8) but using path amounts, ignoring any heterogeneity in the CO_2 distribution. The average flux of all five scans (1055 ± 389 tons/day) is in good agreement with the result obtained from the 2-D map (1106 ± 288 tons/day).. Note that disagreement with the flux result from the 2-D map may partly be due to the frozen plume assumption, since this assumption is better fulfilled for the acquisition

5   of a single 1-D profile, which takes much less time. Future scans shall thus be acquired with higher scan velocity or from further away.

Yet, both the CO_2 flux from the 2-D map and from the 1-D profiles are higher than fluxes previously estimated. To our knowledge, all former studies except one (Pedone et al., 2014) inferred X_{CO_2} and hence CO_2 fluxes from a grid of point measurements, which may have missed degassing activity in between the measurement points and so tended to yield lower

10   flux values. Spatially comprehensive sounding by Pedone et al. (2014) resulted in a CO_2 flux of only ~300 tons/day in early 2013, however, it focused on the area around the Solfatara main vents, that is, 8000 m^2. In this study the area considered for flux computation was over 21000 m^2. The average degassing rate at Solfatara has been increasing by ~9% each year over the past 10 years or so (Chiodini et al., 2010; d'Auria, 2015). Extrapolating the 300 tons/day would yield a flux of 390 tons/day in early 2016. Integrating CO_2 mixing ratios of the area around the main vents only (bounded to the south by in situ point 6,

15   Fig. 6c) yields a flux of 399 ± 104 tons/day of CO_2, in excellent agreement with the extrapolated flux. However, as mentioned before, CO_2 from the main vents mixes with surrounding volcanic CO_2 and furthermore the scans focused on the area south of the main vents (poor ray coverage at BN and BG). So this value should be interpreted with care. It deems to be reasonable to exclude the zone of high anomalous degassing in the north of the 2-D map, which leads to a flux of 675 ± 175 tons/day, representing any degassing activity (vented and diffuse) within the investigated area, excluding the main vent area (BN and

20   BG). This magnitude equals roughly 45% of the total CO_2 flux of the DDS (diffuse degassing structure) reported by Granieri et al. (2003), 13 years prior to this study.

All five scans were performed one-sided, i.e. from a single half space, as often the case in geophysical tomography problems (e.g. Hobro et al., 2003). This is not ideal for any inversion technique as it makes the inverse problem highly non-linear with a non-unique solution, meaning that many models may explain the observed data equally well. However, for

25   Solfatara there is an abundance of hard data available, which extremely facilitated the rejection of unlikely models. This case therefore enabled to demonstrate that one may obtain useful tomographic results from one-sided scanning of a degassing feature. The inverted model is missing small-scale features, since to linearize the inversion the grid spacing had to be rather coarse. Yet, given the fair agreement with the hard data, the inverted 2-D model (Fig. 6c) is quantitatively sound and outlines the geometry of the diffuse degassing probed at Solfatara. Future measurements of this type at Solfatara are envisaged,

30   including a more systematic study, using a wider variety of viewing angles, which will allow a more quantitative picture as to which extent this method is useful for one-sided tomography of highly non-isotropic volcanic CO_2 plumes. In particular, we expect an enlarged angle diversity to increase the maximum number of grids usable for stable inversion, boosting 2-D resolution. The outcome indicates this method to be particularly useful for future measurement campaigns using hard target DIAL to scan volcanic plumes from an aircraft or similar acquisition geometries sensing other types of gas emission.

5 Conclusions

As magmatic CO_2 degassing rates are tracers for the dynamics and chemistry of the magma plumbing system beneath Campi Flegrei and at volcanic areas in general, a comprehensive quantification of magmatic CO_2 degassing strength is of interest for volcanology and of vital importance for civil protection.

Scanning hard target DIAL measurements have been performed at Solfatara crater (Campi Flegrei, Italy), which allowed an inclusive measurement of CO_2 amounts in the form of 1-D profiles of CO_2 path amounts. From the 1-D profiles a 2-D map of CO_2 mixing ratios has been reconstructed outlining the main CO_2 distribution. Such a map is useful to geometrically correct the CO_2 flux obtained from 1-D concentration profiles for heterogeneous CO_2 distribution. Since it was in line with in situ hard data, the 2-D map was directly used to retrieve the CO_2 flux, which is compatible with previous results. The 1-D profiles have been acquired from a single half space, which indicates this tomography method to be beneficial for scanning strongly non-isotropic CO_2 distributions, such as diffuse emissions, that can be viewed from limited angles only. To fully assess the potential of this method, future acquisitions should involve different scanning geometries, potentially allowing for an enhanced resolution of the 2-D map and thus more accurate gas flux estimation.

Acknowledgments

The research leading to these results has received funding from the European Research Council under the European Union's Seventh Framework Programme (FP/2007-2013)/ERC Grant Agreement n. 279802. Our gratitude goes to Rosario Avino and Antonio Carandente (INGV Osservatorio Vesuviano), who sampled the in situ CO_2 mixing ratios. We thank Grant Allen (NASA Goddard) and Luca Fiorani (ENEA) for sharing extremely valuable experiences in LIDAR development with us.

References

Aiuppa, A., Burton, M., Allard, P., Caltabiano, T., Giudice, G., Gurrieri, S., Liuzzo, M., Salerno, G.: First observational evidence for the CO_2-driven origin of Stromboli's major explosions, Solid Earth, 2, 135-142, 2011.

Aiuppa, A., Tamburello, G., Di Napoli, R., Cardellini, C., Chiodini, G., Giudice, G., Grassa, F., and Pedone, M.: First observations of the fumarolic gas output from a restless caldera: Implications for the current period of unrest (2005–2013) at Campi Flegrei, Geochem. Geophys. Geosyst., 14, 4153-4169, 2013.

5 Aiuppa, A., Fiorani, L., Santoro, S., Parracino, S., Nuvoli, M., Chiodini, G., Minopoli, C., and Tamburello, G.: New ground-based lidar enables volcanic CO_2 flux measurements, Sci. Rep., 5, 13614; doi: 10.1038/srep13614, 2015.

Amediek, A., Fix, A., Wirth, M., and Ehret, G.: Development of an OPO system at 1.57 µm for integrated path DIAL measurement of atmospheric carbon dioxide, Appl. Phys. B, 92, 295-302, 2008.

d'Auria, L.: Update sullo stato dei Campi Flegrei, INGV, Sezione di Napoli, Report, available at ftp://ftp.ingv.it/pro/web_ingv/Convegno_Struttura%20_Vulcani/presentazioni/15_D'auria_CampiFlegrei/dauria_cf.pdf, accessed in May 2016, 2015.

15 Bagnato, E., Barra, M., Cardellini, C., Chiodini, G., Parello, F., and Sprovieri, M.: First combined flux chamber survey of mercury and CO_2 emissions from soil diffuse degassing at Solfatara of Pozzuoli crater, Campi Flegrei (Italy): Mapping and quantification of gas release, J. Volcanol. Geotherm. Res., 289, 26-40 2014.

Baubron, J. C., Allard, P., Sabroux, J. C., Tedesco, D., Toutain, J.P.: Soil gas emanations as precursory indicators of
20 volcanic eruptions, J. Geol. Soc. London 148, 571-576, 1991.

Burton, M. R., Sawyer, G. M., and Granieri, D.: Deep carbon emissions from Volcanoes, Rev. Mineral. Geochem., 75, 323-354, 2013.

25 Carapezza, M. L., Inguaggiato, S., Brusca, L., and Longo, M.: Geochemical precursors of the activity of an open-conduit volcano: The Stromboli 2002-2003 eruptive events, Geophys. Res. Lett., 31, L07620, 2004.

Chiodini, G., Baldini, A., Barberi, F., Carapezza, M. L., Cardellini, C., Frondini, F., Granieri, D., and Ranaldi, M.: Carbon dioxide degassing at Latera caldera (Italy): Evidence of geothermal reservoir and evaluation of its potential energy, J. Geophys.
30 Res., 112, B12204, 2007.

Chiodini, G., Caliro, S., Cardellini, C., Granieri, D., Avino, R., Baldini, A., Donnini, M., and C. Minopoli.: Long-term variations of the Campi Flegrei, Italy, volcanic system as revealed by the monitoring of hydrothermal activity, J. Geophys. Res., 115, B03205, doi:10.1029/2008JB006258, 2010.

Chiodini, G., Pappalardo, L., Aiuppa, A., and Caliro, S.: The geological CO_2 degassing history of a long-lived caldera, Geology, 43, 767-770, 2015.

Diaz, J. A., Pieri, D., Arkin, C. R., Gore, E., Griffin, T. P., Fladeland, M., Bland, G., Soto, C., Madrigal, Y., Castillo, D., Rojas, E., and Achi, S.: Utilization of in situ airborne MS-based instrumentation for the study of gaseous emissions at active volcanoes, Int. J. Mass Spectrom., 295, 105-112, 2010.

Dobler, J. T., Harrison, F. W., Browell, E. V., Lin, B., McGregor, D., Kooi, S., Choi, Y., and Ismail, S.: Atmospheric CO_2 column measurements with an airborne intensity-modulated continuous-wave 1.57-micron fiber laser lidar, Appl. Optics, 52, 2874-2894, 2013.

Frezzotti, M.-L. and Touret, J. L. R.: CO_2, carbonate-rich melts, and brines in the mantle, Geosci. Front., 5, 697-710, 2014.

Galle, B., Johansson, M., Rivera, C., Zhang, Y., Kihlman, M., Kern, C., Lehmann. T., Platt, U., Arellano, and S., Hidalgo, S.: Network for Observation of Volcanic and Atmospheric Change (NOVAC)-A global network for volcanic gas monitoring: Network layout and instrument description, J. Geophys. Res., 115, D05304, doi:10.1029/2009JD011823, 2010.

Gerlach, T. M., Delgado, H., McGee, K. A., Doukas, M. P., Venegas, J. J., Cárdenas, L.: Application of the LI-COR CO_2 analyzer to volcanic plumes: A case study, volcán Popocatépetl, Mexico, June 7 and 10, 1995, J. Geophys. Res., 102, 8005-8019, 1997.

Granieri, D., Chiodini, G., Marzocchi, W., and Avino, R.: Continuous monitoring of CO_2 soil diffuse degassing at Phlegraean Fields (Italy): influence of environmental and volcanic parameters, Earth Planet. Sci. Lett., 212, 167-179, 2003.

Granieri, D., Avino, R., Chiodini, G.: Carbon dioxide diffuse emission from the soil: ten years of observations at Vesuvio and Campi Flegrei (Pozzuoli), and linkages with volcanic activity, Bull. Volcanol., 72, 103–118, doi:10.1007/s00445-009-0304-8, 2010.

Granieri, D., Carapezza, M. L., Barberi, F., Ranaldi, M., Ricci, T., and L. Tarchini.: Atmospheric dispersion of natural carbon dioxide emissions on Vulcano Island, Italy, J. Geophys. Res. Solid Earth, 119, doi:10.1002/2013JB010688, 2014.

Hards, V. L.: Volcanic contributions to the global carbon cycle, British Geological Survey Occasional Report No. 10, 26pp., 2005.

Hobro, J. W. D., Singh, S. C., and Minshull, T. A.: Three-dimensional tomographic inversion of combined reflection and refraction seismic traveltime data, Geophys. J. Int., 152, 79-93, 2003.

5   Johansson, M., Galle, B., Rivera, B., and Zhang, Y.: Tomographic reconstruction of gas plumes using scanning DOAS, Bull. Volcanol., 71, 1169-1178, 2009.

Kameyama, S., Imaki, M., Hirano, Y., Ueno, S., Kawakami, S., Sakaizawa, D., and Nakajima, M.: Development of 1.6 µm continuous-wave modulation hard-target differential absorption lidar system for CO_2 sensing, Opt. Lett., 34, 1513-1515, 2009.

Kazahaya, R., Mori, T., Kazahaya, K., and Hirabayashi, J.: Computed tomography reconstruction of SO_2concentration distribution in the volcanic plume of Miyakejima, Japan, by airborne traverse technique using three UV spectrometers, Geophys. Res. Lett., 35, L13816, 2008.

15   Koch, G. J, Barnes, B. W., Petros, M., Beyon, J. Y., Amzajerdian, F., Yu, J., Davis, R. E, Ismail, S., Vay, S., Kavaya, M. J, and Singh, U. N.: Coherent differential absorption lidar measurements of CO_2, Appl. Optics, 43, 5092-5099, 2004.

La Spina, G., Burton, M., and de Vitturi, M.: Temperature evolution during magma ascent in basaltic effusive eruptions: A numerical application to Stromboli volcano, Earth Planet. Sci. Lett., 426, 89-100, 2015.

Lee, H, Muirhead, J. D, Fischer, T. P, Ebinger, C. J, Kattenhorn, S. A, Sharp, Z. D., and Kianji, G.: Massive and prolonged deep carbon emissions associated with continental rifting, Nature Geosci., 9, 145-149, 2016.

Lewicki, J. L., Bergfeld, D., Cardellini, C., Chiodini, G., Granieri, D., Varley, N., Werner, C.: Comparative soil CO_2 flux
25   measurements and geostatistical estimation methods on Masaya volcano, Nicaragua, Bull. Volcanol., 68, 76-90, 2005.

McGee, K. A., Doukas, M. P., McGimsey, R. G., Neal, C. A., and Wessels, R. L.: Atmospheric contribution of gas emissions from Augustine volcano, Alaska during the 2006 eruption, Geophys. Res. Lett., 35, L03306, doi:10.1029/2007GL032301, 2008.

30

MacKerrow, E. P, Schmitt, M. J., and Thompson, D. C.: Effect of speckle on lidar pulse-pair ratio statistics, Appl. Optics, 36, 8650-8669, 1997.

Menzies, R. T. and Chahine, M. T.: Remote Atmospheric Sensing with an Airborne Laser Absorption Spectrometer, Appl. Opt., 13, 2840-2849, 1974.

Oliver, M. A.: Kriging: a method of estimation for environmental and rare disease data, Geo. Soc., London, Special Publications, 113, 245-254, doi: 10.1144/GSL.SP.1996.113.01.21, 1996.

Pedone, M., Aiuppa, A., Giudice, G., Grassa, F., Cardellini, C., Chiodini, G., and Valenza, M.: Volcanic CO_2 flux measurement at Campi Flegrei by Tunable Diode Laser absorption Spectroscopy, Bull. Volc., 76, doi: 10.1007/s00445-014-0812-z, 2014.

Platt, U., Lübke, P., Kuhn, J., Bobrowski, N., Prata, F., Burton, M., Kern, C.: Quantitative imaging of volcanic plumes -Results, needs, and future trends, J. Volcanol. Geotherm. Res., 300, 7-21, 2015.

Petrazzuoli, S. M., Troise, C., Pingue, F., and DeNatale, G.: The mechanisms of Campi Flegrei unrests as related to plastic behaviour of the caldera borders, Ann. Geofis., 42, 529-544, 1999.

Queißer, M. and Singh, S. C.: Full Waveform Inversion for time lapse quantitative monitoring of CO_2 storage, Geophys. Prosp., 61, 537-555, 2012.

Queißer, M., Burton, M., and Fiorani, L.: Differential absorption lidar for volcanic CO_2 sensing tested in an unstable atmosphere, Opt. Express, 23, 6634-6644, 2015a.

Queißer, M , Granieri, D., Burton, M., La Spina, A., Salerno, G., Avino, R., and Fiorani, L.: Intercomparing CO_2 amounts from dispersion modeling, 1.6 µm differential absorption lidar and open path FTIR at a natural CO_2 release at Caldara di Manziana, Italy, Atmos. Meas. Tech. Discuss., 8, 4325-4345, 2015b.

Rothman, L. S., Gordon, I. E., Babikov, Y., Barbe, A., Benner, D. C., Bernath, P. F., Birk, M, Bizzocchi, L., Boudon, V., Brown, L. R., Campargue, A., Chanc, K., Coudert, L., Devi, V. M., Drouin, B. J., Fayt, A., Flaud, J.-M., Gamache, R. R., Harrison, J., Hartmann, J.-M., Hill, C., Hodges, J. T., Jacquemart, D., Jolly, A., Lamouroux, J., LeRoy, R. J., Li, G., Long, D., Mackie, C. J., Massie, S. T., Mikhailenko, S., Müller, H. S. P., Naumenko, O. V., Nikitin, A. V., Orphal, J., Perevalov, V., Perrin, A., Polovtseva, E. R., Richard, C., Smith, M. A. H., Starikova, E., Sung, K., Tashkun, S., Tennyson, J., Toon, G. C., Tyuterev, V. G., Auwera, J. V., and Wagner, G.: The HITRAN 2012 Molecular Spectroscopic Database, J. Quant. Spectrosc. Ra., 130, 4-50, 2013.

Sakaizawa, D., Nagasawa, C., Nagai, T., Abo, M., Shibata, Y., Nakazato, M.,and Sakai, T.: Development of a 1.6 µm differential absorption lidar with a quasi-phase-matching optical parametric oscillator and photon-counting detector for the vertical CO_2 profile, Appl. Optics, 48, 748-757, 2009.

5   Sakaizawa, D., Kawakami, S., Nakajiama, M., Tanaka, T., Morino, I., and Uchino, O.: An airborne amplitude modulated 1.57 µm differential laser absorption spectrometer: simultaneous measurement of partial column-averaged dry air mixing ratio of CO_2 and target range, Atmos. Meas. Tech., 6, 387-396, 2013.

Scarpati, C., Cole, P., and Perrotta, A.: The Neapolitan Yellow Tuff- A large volume multiphase eruption from Campi Flegrei,
10   Southern Italy, Bull. Volcanol., 55, 343-356, 1993.

Tassi, F, Nisi, B., Cardellini, C., Capecchiacci, F., Donnini, M., Vaselli, O., Avino, R., and Chiodini, G.: Diffuse soil emission of hydrothermal gases (CO_2, CH_4 and C_6H_6) at the Solfatara crater (Phlegraean Fields, southern Italy), Appl. Geochem., 35, 142-153, 2013.

Weibring, P., Edner, H., Svanberg, S., Cecchi, G., Pantani, L., Ferrara, R., Caltabiano, T.: Monitoring of volcanic sulphur dioxide emissions using differential absorption lidar (DIAL), differential optical absorption spectroscopy (DOAS), and correlation spectroscopy (COSPEC), Appl. Phys. B, 67, 419-426, 1998.

20   Wright, T. E., Burton, M. R., Pyle, D. M, and Caltabiano, T.: Scanning tomography of SO_2 distribution in a volcanic gas plume, Geophys. Res. Lett., 35, L17811, doi: 10.1029/2008GL034640, 2008.

25

30

Figures
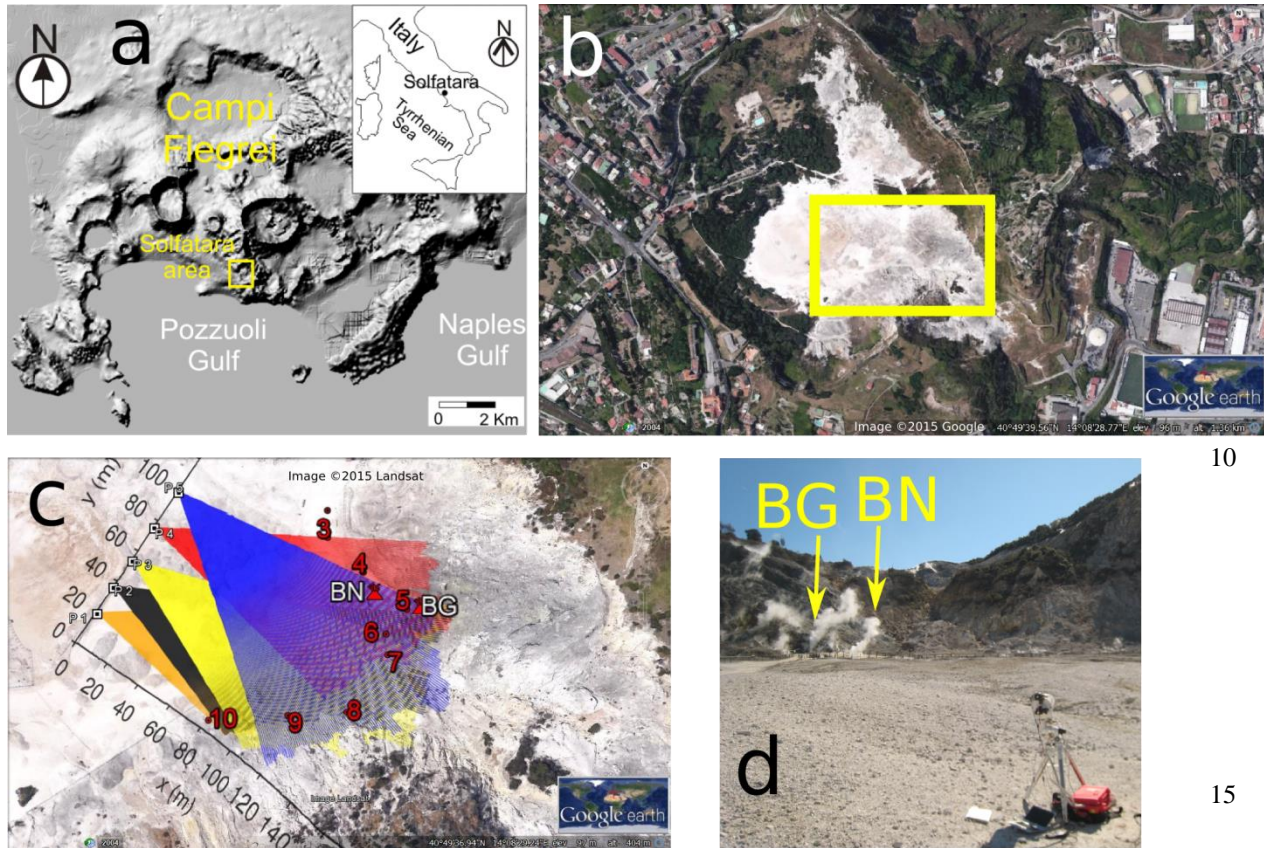
Figure 1: Geography and measurement geometry. (a) Location of the Solfatara crater as part of the volcanic area of Campi Flegrei, near Naples (Italy). (b) Nadir photo of Solfatara crater. The rectangle contains the region of interest. (c) Zoom of area outlined by the rectangle depicting the five instrument positions P1 to P5 with the following UTM-coordinates: P1: (427476, 4519921), P2: (427485, 4519935), P3: (427495, 4519949), P4: (427507, 4519967), P5: (427520, 4519986). Also shown are the respective range vectors (rays) for all five scans and the numbered locations of the LICOR measurements. (d) Photo taken during the scan at P5 looking towards east. The largest clouds of condensed water aerosol appeared near the main vents (Bocca Nuova, BN and Bocca Grande, BG) on the left. The CO₂DIAL, visible in the lower right corner, comprised of the tripod carrying the telescope (with transmitter unit) and the main unit (red box).
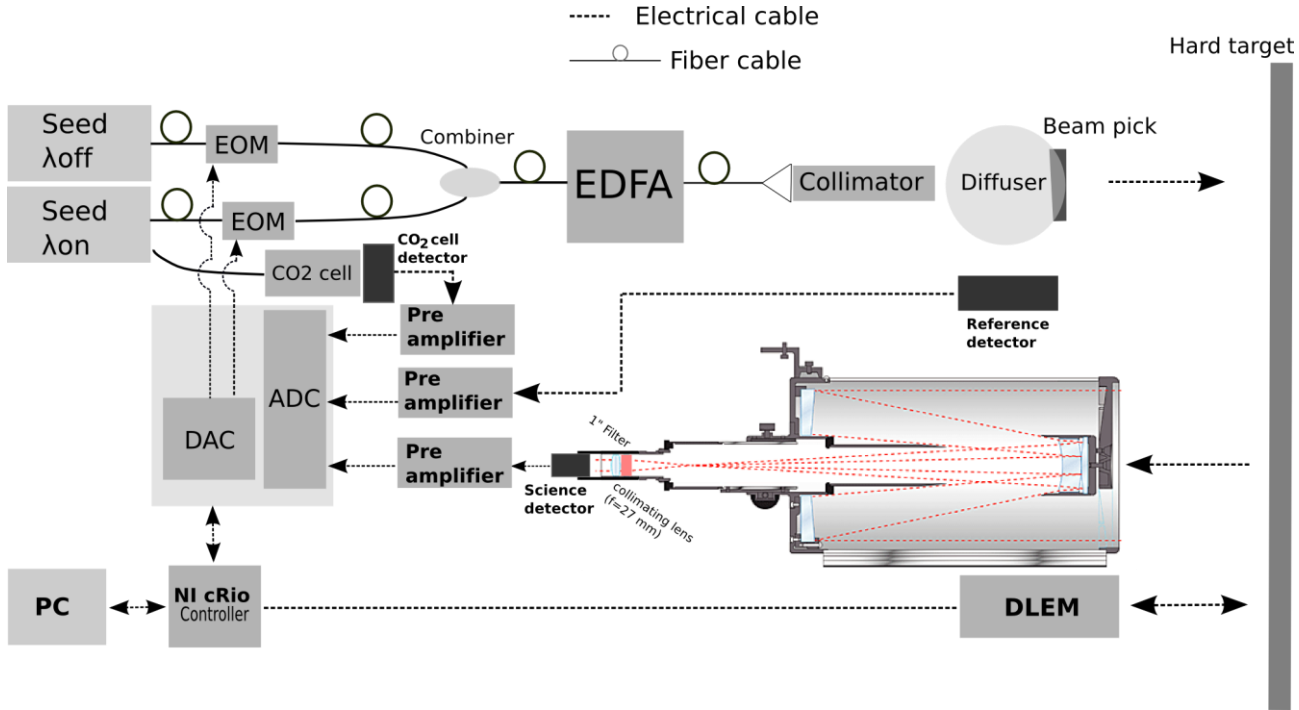
Figure 2: Scheme of the CO₂ DIAL as used for this experiment. EOM: Electro-optical modulator, DLEM: range finder module, EDFA: Erbium doped fiber amplifier. ADC: analog-to-digital converter, DAC: digital-to-analog converter. The CO₂ cell is used to
5 **calibrate the seed laser wavelengths. To minimize hard target and turbulence related speckle noise the collimator used had a relatively high divergence of 1.7 mrad while the telescope field of view was 1.5 mrad. For mechanical reasons the optical band pass filter was mounted before the collimating lens. The change in transmission spectrum can be neglected.**
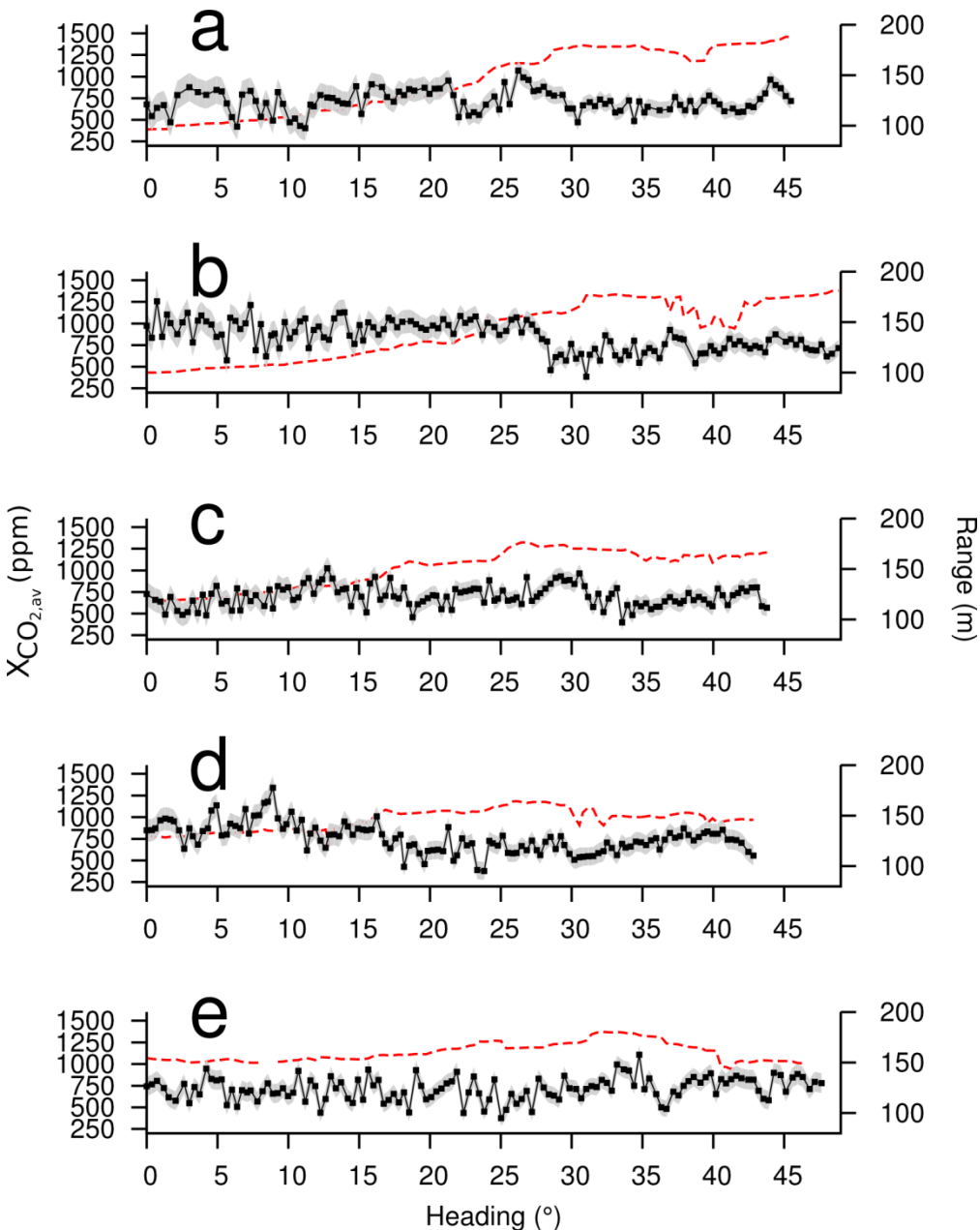
Figure 3: 1-D profiles of $X_{CO_2,av}$, the total (not background corrected) CO_2 mixing ratios, derived by dividing the path amounts $X_{CO_2}^{col}$ (ppm.m) per angle by the associated range. Each value therefore represents a column-averaged concentration. Each point corresponds to 784 ms integration time. For each profile and heading ranges are indicated by the red dashed line. (a) Profile acquired between 9:35:36 and 9:41:54. (b) Profile acquired between 10:04:08 and 10:10:54. (c) Profile acquired between 10:31:24 and 10:37:28. (d) Profile acquired between 11:01:46 and 11:07:46. (e) Profile acquired between 11:50:39 and 11:57:15. The grey envelope depicts precision (1 SD, Eq. 3).
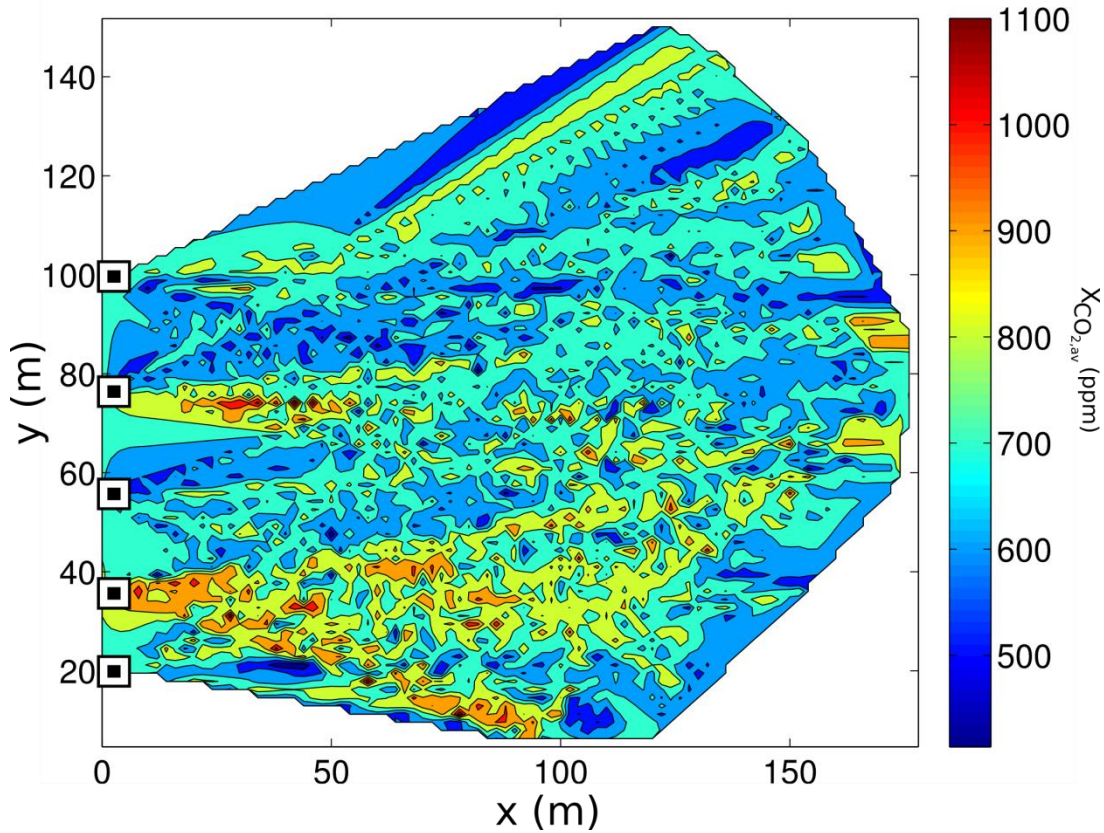
Figure 4: Contour plot of $X_{CO_2,av}$ ($X_{CO_2}^{col}$ divided by the range) for all 627 beam paths. Also shown are the instrument positions (squares on y-axis) starting with P1 at $y = 20$ m. The data has been regridded on a regular grid of 90×90 points using natural interpolation. One would expect high anomalous CO_2 mixing ratios near the main vents (BN, BG near $x = 120$ m, $y = 140$ m) and the southern part of the area. Low anomalous CO_2 mixing ratios are to be expected in the northwestern part. Note that due to the abundance of data some data points were masking each other. They were thus averaged, leading to a maximum mixing ratio lower than actually observed (e.g. in Fig. 3b).

25
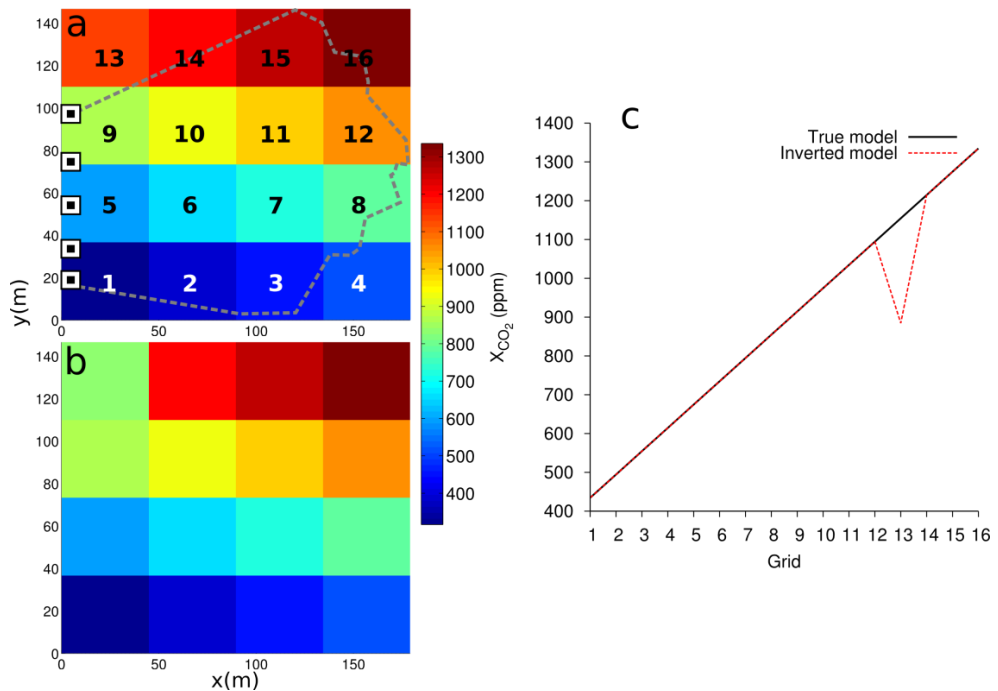
Figure 5: Synthetic inversion result with $n = 16$ grid cells. (a) True model used to generate synthetic column averaged $X_{CO_2}^{col}$. Each grid cell is identified by a grid number. The dotted line outlines the ray coverage. The instrument positions are indicated. (b) Inverted model. (c) True and inverted X_{CO_2} versus grid cell. The inverted X_{CO_2} for grid 13 is off since the ray coverage associated with that area was poor.
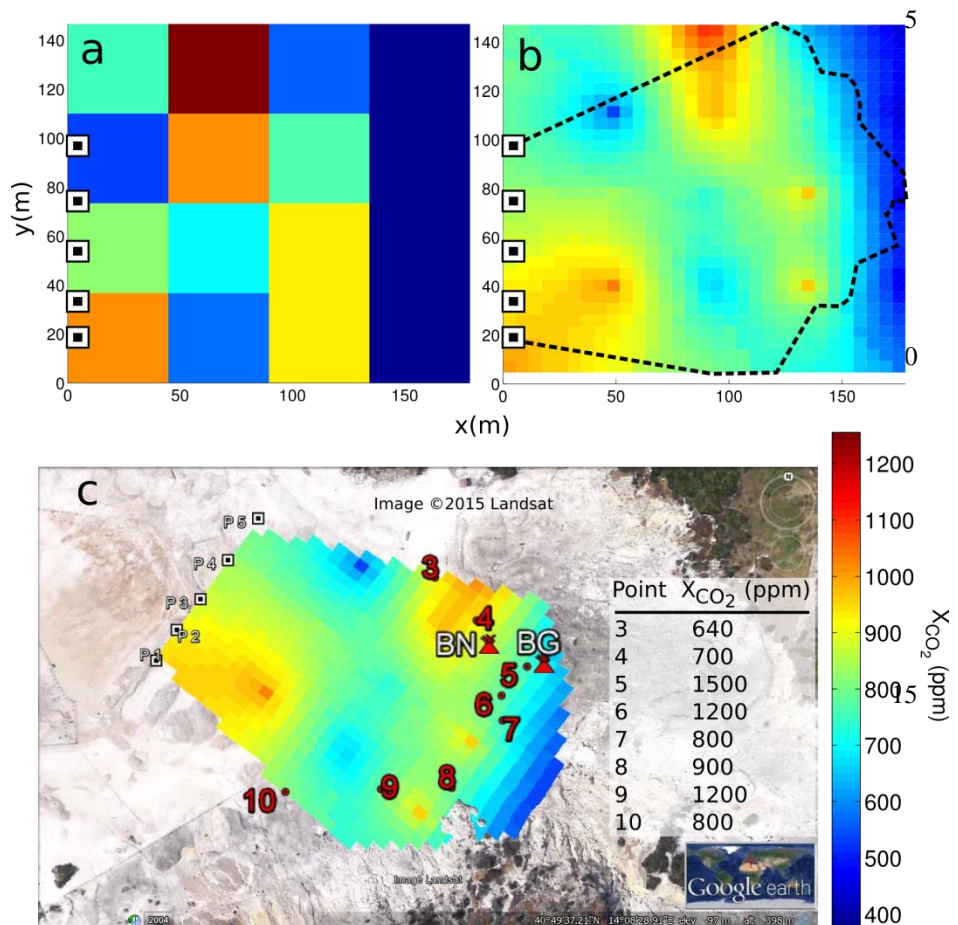
20 **Figure 6: Retrieved 2-D model of X_{CO_2}. (a) Inverted model of X_{CO_2}. (b) Inverted X_{CO_2} in after ordinary Kriging interpolation. The ray coverage is depicted by the dotted line. (c) X_{CO_2} superposed onto nadir photo of Solfatara for those grid cells covered by the rays. Also shown are the X_{CO_2} from in situ measurements (measurement points 3 to 10) using the LICOR CO_2 analyzer. Note that the in situ values had been acquired a day before the scans and thus serve as an approximate reference only.**